NEW EXPERIMENTAL CONSTRAINTS ON REE PARTITIONING BETWEEN APATITE AND SILICATE MELTS AND A TEMPERATURE AND COMPOSITION-DEPENDENT PREDICTIVE PARTITIONING MODEL

D. Ji, N. Dygert, Department of Earth and Planetary Sciences, University of Tennessee (dji2@vols.utk.edu).

Introduction: Apatite [$Ca_5(PO_4)_3$(OH, F, Cl)] is an omnipresent accessory mineral in different kinds of rocks on Earth as well as other bodies in the Solar System [e.g., 1]. This work presents results of new apatite-melt partitioning experiments relevant to the lunar magma ocean (LMO), and a novel predictive model for apatite-melt trace element partitioning. Although representing a small proportion of the rock and acting as a late-crystallizing mineral, apatite can harbor essential amounts of REEs (rare earth elements) and other trace elements in magmatic systems. Apatites have been discovered in returned Apollo samples [e.g., 2-4] and also occur in experiments representing the late stages of LMO crystallization [e.g., 5, 6]. Since apatite has much higher partition coefficients for REEs than major minerals, it has enormous potential to control bulk elemental partitioning and affect elemental concentrations in major minerals during LMO solidification and subsequent geological events (e.g., partial melting, subsolidus reequilibration).

In the apatite structure, forty percent of the Ca atoms occupy the larger lattice site (nine-fold coordination, Ca1 site), while the rest enter the seven-fold coordinated site (Ca2 site), surrounding the F (OH, Cl) (X-site). Because of the similarity of ion radius, REEs substitute for Ca^{2+} ions. Researchers found that REE occupancy may depend on the anion occupancy on the X site [7]. For three endmembers of apatite, i.e., fluorapatite, hydroxylapatite and chlorapatite (FlAp, OHAp and ClAp), previous studies reveal that temperature [8], as well as the polymerization of the melt [9, 10], have huge impacts on REE partition coefficients, however, because of the lack of data, relationships between the X-site occupancy (F, OH, Cl) and the REE partitioning parameters could not be quantified. In order to address the effect of anionic occupancy on apatite-melt partitioning, we experimentally determine REE partition coefficients as a function of temperature and oxygen fugacity between apatite and silicate melts for all FlAp, OHAp, and ClAp and develop lattice strain-based predictive partitioning model for REEs using the new and previously published data.

Methods: *Starting materials*. Three different starting materials were used in our experiments with the same bulk composition with the exception of the anionic component (39.77 wt% SiO_2, 3.52 wt% TiO_2, 5.93 wt% Al_2O_3, 32.88 wt% FeO, 0.66 wt% MnO, 0.89 wt% MgO, 11.36 wt% CaO, 0.52 wt% Na_2O, 0.24 wt% K_2O, 4.22 wt% P_2O_5, and 0.28, 0.32, and 0.59 wt% F, Cl and OH respectively). Starting materials were prepared by grinding reagent grade oxide and carbonate powders into three separate homogeneous mixtures, then decarbonating the mixtures in an 850 °C furnace overnight. We conditioned each mixture in a gas mixing furnace for 4 hours according to the target fO_2 of the experiment. Synthetic $Ca_5(PO_4)_3OH$, CaF_2 and NaCl were then added into the mixtures to keep the molar percentage of F, Cl, OH, as well as other cations in each starting material the same.

Experimental procedures. Nine piston-cylinder experiments were conducted at the University of Tennessee. In the first six experiments, Mo capsules with graphite liners were used to produce three endmember apatites (OHAp, FlAp and ClAp) at different temperatures at fO_2s close to IW-1 [12]. In three additional experiments, a similar assembly design was used, but also containing a layer of Cr metal powder isolated from the experimental powders and outer jackets by layers of graphite to maintain the fO_2 close to IW-5 [13]. Experiments were conducted at 1 GPa and 1050-1100 °C for 48 to 76 h. A representative image of the experiments is shown in Fig.1.

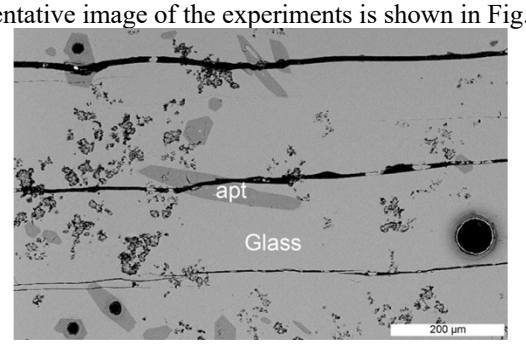

Fig.1. Backscatter photomicrograph of experiment OHAp-6. The black circles represent laser ablation pits. Apt represents apatite.

Analytical techniques. Major element compositions were characterized using a Cameca SX-100 electron microprobe (EMP) at the University of Tennessee. The standards used are fluorapatite and HgCl for apatite X-site occupancy, with mass deficit used to characterize the OHAp component. The analytical uncertainty of Cl is hundreds of ppm while that of F is thousands of ppm. Trace element concentrations in apatite and glass were determined by laser ablation inductively coupled plasma mass spectrometry (LA-ICP-MS) at the University of Texas at Austin. The analytical spot sizes of apatite vary from 15 to 20 µm, while those for glass are 30 and 60 µm.

Results: Using the data acquired by LA-ICP-MS analysis, we calculate partition coefficients for REEs between apatite and silicate melts (Fig. 2). Surprisingly, ClAp has lowest REE partition coefficients, as well as positive Eu anomalies, compared with FlAp and OHAp. Temperature also affects the partition coefficients, as the experiments show that the lower the temperature, the higher the partition coefficient, as suggested by [9]. In lower fO_2 experiments (IW-5), the partition coefficients of Eu decrease. No systematic effect of fO_2 on the partition coefficients of other REEs was observed.

Partitioning behavior can be effectively described using the lattice strain model [e.g., 14]:

$$D_i^{min-melt} = D_o exp\left[\frac{-4\pi E N_A}{RT}\left(\frac{r_o}{2}(r_o - r_i)^2 - \frac{1}{3}(r_o - r_i)^3\right)\right] \quad (1)$$

where $D_i^{min-melt}$ is the mineral-melt partition coefficient of element i; D_o is the strain free partition coefficient; E is the effective Young's modulus; r_o is the ideal ionic radius; r_i is the ionic radius of substituting element; R is the gas constant; N_A is Avogadro's number and T is the temperature in kelvin.

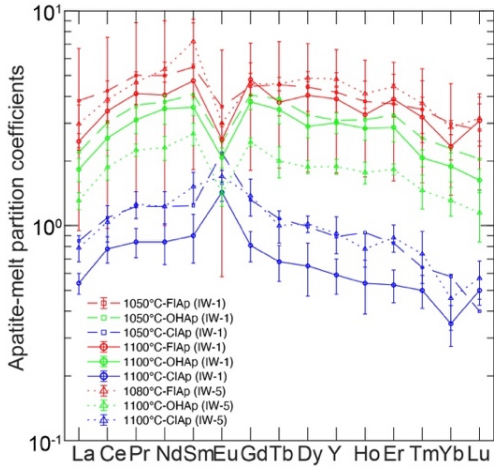

Fig. 2. Apatite-silicate melt partition coefficients calculated based on LA-ICP-MS analysis. Solid lines show experiments conducted at higher T and IW-1. Lowest T experiments are plotted using dashed lines and low fO_2 experiments are plotted using dotted lines.

The lattice strain parameters can be estimated by non-linear least squares regression based on experimentally determined partition coefficients of isovalent cations. More details about the modeling methods are in [15]. The predictive partitioning model for REEs we developed has the form:

$$ln D_o^{3+} = a_0 + \frac{a_1}{RT} + a_2 X_{Ca} + a_3 X_{Si} + a_4 X_P \quad (2)$$

$$E^{3+} = a_5 + a_6 X_P + a_7 X_P + a_8 X_{Si} \quad (3)$$

$$r_o^{3+} = a_9 + a_{10} X_P \quad (4)$$

where X_{si}, X_{Ca} and X_P are the Si, Ca and P contents in apatite per 12.5 oxygen, and the a_n coefficients are determined by the nonlinear regression.

Discussion: The REE partition coefficients of OHAp and FlAp are similar at a given temperature; those for ClAp are a factor of two to four lower depending on the experiment. Single-crystal X-ray refinement studies have shown that REEs prefer the Ca2 site in FlAp and OHAp [7]. Because the radius of Cl^- is larger than that of F^- and OH^-, in ClAp the REEs partition into the Ca1 site, which accommodates proportionally more light-REEs than the Ca2 site, as suggested by higher D_{La} / D_{Yb} in ClAp experiments at a given temperature. Because the radii of F^- and OH^- are similar, the REE partitioning behavior of OHAp and FlAp are very similar.

In our predictive model, the Si, Ca and P contents in apatite play an important role in the partitioning behavior of REEs, which can be explained by following two substitution mechanisms: $REE^{3+} + Si^{4+} = Ca^{2+} + P^{5+}$ [e.g., 9], and $2REE^{3+} + [v] = 3Ca^{2+}$ [e.g., 16], where [v] represents a cation vacancy. The above mechanisms are suggested by correlations between REE concentration in apatite and Ca and P concentration in apatite and Si concentration in melt. Si in apatite is inversely correlated with Si in coexisting melt [10], justifying the lack of melt composition dependence of our predictive model.

Application: The slope of the REE partition coefficients across the lanthanides is distinct for ClAp compared to OHAp and FlAp. To explore consequences of potential apatite species on lunar trace element patterns, we use Rapp and Draper's LMO crystallization sequence [5] to calculate trace element fractionation during LMO solidification, assuming that the apatite reaches saturation at 97% solid. We find that the compositions of the LMO residual liquid are similar under the assumption that different species of apatite are crystallized, but the compositions of the remelts of late LMO cumulates are very different among the apatite species, especially for light REEs (Fig. 3A). If the apatite species is closer to the ClAp endmember, remelting of late LMO cumulates overestimates light REEs compared to KREEP basalt. However, remelts produced when apatites are assumed to be FlAp or OHAp fit the KREEP basalts very well, including their Eu anomalies (Fig. 3B; an fO_2-dependent Eu-in-apatite partitioning model will be presented elsewhere). This conclusion is consistent with the analysis of the apatite species in returned Apollo samples [e.g., 4]. Based on the REE patterns of KREEP basalts, we infer a high (F+OH)/Cl LMO, distinct from chondritic precursor materials.

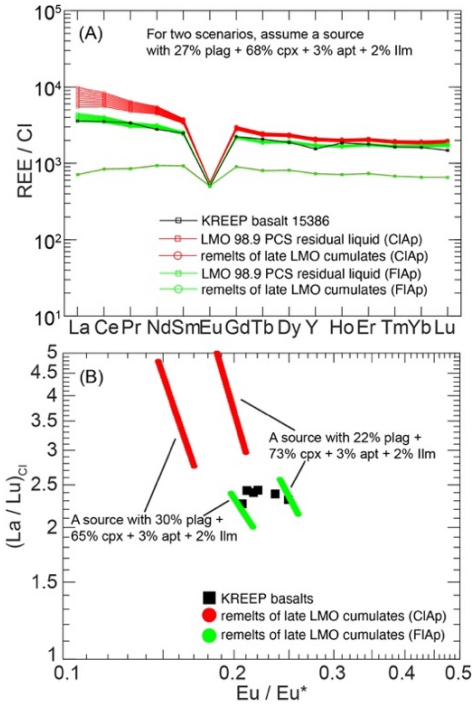

Fig.3. (A) Chondrite-normalized REE patterns of residual liquids after 98.9 percent solidification of the LMO, and remelts of late LMO cumulates compared to KREEP basalt 15386 [17], and (B) $(La / Lu)_{CI}$ versus Eu / Eu* (Eu* is the interpolated value from neighboring elements on a REE diagram) showing remelts of late LMO cumulates with different source mineral modes and apatite species compared to KREEP basalts [17-20].

References: [1] McCubbin & Jones (2015) *Elements* **11**, 183-188. [2] Shervais et al. (1984) *JGR: Solid Earth* **89**, C25-C40. [3] Tartèse et al. (2014) *Geology* **42**, 363-366. [4] Potts et al. (2018) *GCA* **230**, 46-59. [5] Rapp & Draper (2018) *MAPS* **53**, 1452-1455. [6] Schmidt & Kraettli (2022) *JGR: Planets*, e2022JE007187. [7] Pan & Fleet (2002) *RMG* **48**, 13-49. [8] Li & Hermann (2017) *CG* **473**, 55-73. [9] Watson & Green (1981) *EPSL* **56**, 405-421. [10] Prowatke & Klemme (2006) *GCA* **70**, 4513-4527. [11] Chen et al. (2016) *Lithos* **266**, 435-452. [12] Dygert et al. (2014) *GCA* **132**, 170-186. [13] Holzheid & O'Neill (1995) *GCA* **59**, 475-479. [14] Blundy & Wood (1994) *Nature* **372**, 452-454. [15] Yao et al. (2012) *CMP* **164**, 261-280. [16] Chen et al. (2002) *AM* **87**, 47-55. [17] Neal & Kramer, (2003) *LPSC*. [18] Helmke et al., (1973) *The Moon* **8**, 129-148. [19] Hubbard et al. (1973) *LPSC*. [20] McKay et al. (1979) *LPSC*.